

# Molecular dynamics simulations of the defect evolution in tungsten on successive collision cascades

Utkarsh Bhardwaj<sup>a</sup>, M Warriar<sup>a,b</sup>

<sup>a</sup>Computational Analysis Division, BARC, Visakhapatnam, Andhra Pradesh, India – 530012

<sup>b</sup>Homi Bhabha National Institute, Anushaktinagar, Mumbai, Maharashtra, India – 400094

---

## Abstract

Molecular dynamics (MD) simulations of successive collision cascades within the same simulation domain were performed using two different inter-atomic potentials (IAP) in tungsten, one EAM based and the other a ‘quantum accurate’ machine learning potential, SNAP. The micro-structural changes are analyzed as a function of displacements per atom (dpa) for primary knock-on atom (PKA) energies of 20 keV and 50 keV, reaching up-to irradiation dose of 0.1 and 0.2 dpa, respectively. Five sample simulations are carried out for each case for observing stochastic differences in the evolution of damage. A detailed defect analysis is carried out to observe changes in different parameters such as the number of surface defects, defect density, defect morphology and size distribution etc., as a function of dpa. We explore the properties that are sensitive to the IAP used and those that are sensitive to the PKA energy and note their similarities with experimental results at various dpa values. The SNAP potential shows better agreement with the experiments for swelling and number of surface defects. However, it also predicts presence of high number of small sessile defects which may have definite affect on the processes of microstructural evolution and material properties.

*Keywords:* collision cascades, irradiation, defects, defect clusters, molecular dynamics (MD), LAMMPS, Tungsten

---

## 1. Introduction

Irradiation induced changes in materials have been studied at multiple scales for several decades ([1–4] and references therein). The main focus of these studies have been on understanding the change in micro-structure of the materials due to irradiation. Primary damage at the atomistic scales due to collision cascades has been extensively studied ([5–7]). The number of defects, their in-cascade clustering, defect morphologies, cascade properties, etc., are being studied from MD collision cascade databases [8–13]. More recently the effect of IAP used on the primary damage is being explored [7, 14–18]. The evolution of the micro-structure is being studied using kinetic Monte Carlo (KMC) methods [19, 20] and mean field rate theoretical (MFRT) methods [4]. The KMC methods use approximations for the migration energies of diffusion and morphological transitions, and interactions of defects with different morphologies and sizes. KMC methods are also limited in their scale since only small regions of the order of microns can be simulated up-to small doses (fraction of a dpa) [19]. The MFRT methods average over the spatial and temporal variations of the defect distribution and is less exact than the KMC methods, but can handle large regions for high doses [4].

---

*Email addresses:* haptork@gmail.com (Utkarsh Bhardwaj), manoj.warrier@gmail.com (M Warriar)

It is important to study the stability of the defect clusters [21, 22] their transport, their interactions with each other in order to understand the evolution of the micro-structure due to irradiation.

Another approach used to quantify the irradiation exposure of materials is to define a unit that is physically related to the damage mechanism called "displacements per atom" (dpa) [23]. dpa contains information about both the fluence and the energy of the irradiating particle and is therefore a much better measure than the fluence (fig.1 of [24]). A simple formula, called the NRT-DPA, based on the available energy per primary knock-on atom (PKA) and accounting for the displacement efficiency, electronic stopping and the displacement energy required to create a Frenkel Pair, was developed as a standard for evaluating dpa [25]. The NRT-DPA, which is the current standard for quantifying energetic particle damage to materials for the past four decades, has several shortcomings like (i) over-estimating the number of Frenkel pairs produced and (ii) under-estimating the number of atoms replaced in the lattice [26]. Therefore newer, more accurate models, have been proposed [26–28].

The studies at multiple scales mentioned in the first paragraph have yielded insights into irradiation induced damage. However, a lot more work on the stability, transport and interactions of defects have to be carried out using MD to be able to model micro-structure evolution due to irradiation accurately with higher scale models. A recent approach to straddle over this shortcoming is based on the fact that the material properties show a good correlation with dpa. Several researchers have created dpa at the atomic level by a combination of random Monte Carlo moves of atoms followed by a conjugate gradient relaxation of the atomic positions called the creation relaxation algorithm (CRA) [29, 30]. Mason et al. have got better results by introducing a molecular dynamics collision cascade cascade in-between several Monte Carlo steps [30]. Byggmästar et al., have studied the effect of IAP on the evolution of defects at high doses by carrying out successive MD simulations of collision cascades in W at 10 keV [14]. They have validated their results by using machine-learning (ML) interatomic potential for relaxation of simulation cells that are obtained using non-ML interatomic potentials. The ML interatomic potential is considered quantum accurate but relatively slow to carry out high-dose irradiation simulations.

The experiments using techniques such as TEM [31, 32], Transient Grating Spectroscopy (TGS) [33] etc. have recorded important microstructural properties on irradiation such as defect concentration, dislocation densities, swelling etc. at various dpa including lower dpa that can be used to match against the simulation studies.

In this paper we carry out MD simulations of successive collision cascades (SCC) using two different interatomic potentials and at two different PKA energies. We investigate different defect properties as a function of DPA reaching upto 0.1 dpa for 20 keV and 0.2 dpa for 50 keV collision cascades. In the next section we describe the simulations and methods. This is followed by the sections describing our results and discussing them further. Finally the conclusions are presented.

## **2. Methods**

### *2.1. MD Simulations of Successive Collision Cascades*

MD simulations of successive collision cascades were carried out at PKA energies of 20 keV and 50 keV in a simulation domain consisting of  $100 \times 100 \times 100$  unit cells of tungsten using two different IAP. One of the potentials is an embedded atom method (EAM) based potential called the DND-BN potential [34], and the other is a machine learning (ML) based quantum accurate potential called the SNAP potential

[35]. Both the potentials take care that the pair interactions when the atoms in the solid come close to each other are treated by the universal ZBL potential [36]. The simulation region is first equilibrated at zero pressure and 300 K temperature using a NPT ensemble, with periodic boundary conditions (PBC) along all the three directions. After equilibration, a randomly selected PKA is launched in a random direction. The random directions are chosen by identifying uniformly distributed points on a random sphere centered at the position of the PKA. PBC are used for the collision cascade simulations too with a varying time-step such that the fastest atom in the system moves less than 0.1 Å. Electronic stopping is included as a frictional term calculated by the Lindhard-Scharff model [37]. The collision cascade simulations are carried out for 20 ps using an NVE ensemble. Each cascade simulation is followed by an NPT simulation at zero pressure and 300 K temperature for 10 ps to relax the damage. Five trials of successive collision cascade simulations were carried out at each energy and for each potential for statistics. The dpa is calculated using the standard NRT equation [24] with threshold displacement energy of 70 eV [33].

## 2.2. Analysis of the micro-structure damage

The parallelized version of CSaransh [12], a software suite to analyze large database of MD simulations of collision cascades, was used to analyze the simulation results. It outputs various defect properties such as the number of defects, defects in clusters, the defect morphology and size distributions. We analyze the simulation box after every collision cascade for all the five trials which makes a total of 45000 simulation frames to analyze.

A number of factors make analysing high dose SCC simulations particularly more challenging compared to the single PKA simulations. The boundaries in current SCC simulations are not fixed which may result in the movement of whole lattice structure. Due to this global shift in positions the methods that use initial lattice positions as template to find defects such as Wigner-Sietz become infeasible. The presence of large defects sometimes wrapping across the boundary makes it even more difficult to estimate the absolute perfect lattice positions to compare with. The defect analysis algorithms of Csaransh named as AnuVikar use specific minimization methods to make this estimation efficient as well as accurate at such a large scale of analysis. The calculation of different defect morphologies and properties associated with them such as the total defects and surface defect atoms in a dislocation loop are not directly available from the existing algorithms.

The Csaransh software suite used in our study uses, Anuvikar algorithm, a modification of W-S and ES methods [10] to find defects. The algorithm does not take an initial set of positions as input template in case of known crystal structures such as bcc, fcc, hcp etc. The initial position of the beginning of lattice is estimated by optimizing on all the atomic positions. This makes it work well for successive collision cascades where the lattice can shift as a whole and there is a possibility of volumetric swelling. Each atomic coordinate is then associated with its nearest lattice site using modular arithmetic which is more efficient than making geometric structures or neighbour lists as done in W-S method [10]. The lattice sites that are not marked as the nearest lattice site by any atom are vacancies and the atoms that are associated with over-occupied lattice sites are SIAs (self-interstitial atoms) or displaced atoms. We use SaVi, a computational graph based algorithm [10, 11] to classify defect morphologies. It characterizes the orientation and internal morphology of the defects into various classes using computational graphs and computational geometry. The detailed analysis allows calculating the surface defects in a dislocation loop which we use for experimental comparison. It has recently been parallelized for quick analysis of a large database of MD simulations using C++ and python and can typically carry out the analysis of thousands of MD collision cascade atomic positions output in less than an hour and outputs JSON (JavaScript Object Notation) files for further specific analysis.

### 3. Results

We perform subsequent collision cascade simulations at two energies viz. 20 keV and 50 keV, reaching at the approximate dpa levels of 0.1 and 0.2, respectively. Table.1 shows the dpa obtained by the MD simulations for each of the PKA energies and IAP explored. For each case we have performed five sample runs for statistics. Most of the plots in the results section show mean of these five samples along with error bars.

Table 1: The dpa obtained from the successive MD simulations of collision cascades

PKA Energy (keV)	IAP used	Number of PKA Launched	dpa
20	DND-BN	2500	0.11
20	SNAP	2500	0.11
50	DND-BN	2000	0.22
50	SNAP	2000	0.22

#### 3.1. Defect Count

Fig.1 (a) shows the variation of the number of defects per atom as a function of dpa. Fig. 1 (b) includes the single point defects and only the surface atoms of an interstitial defect cluster. It is same as counting the point defects at the boundary or around the dislocation loop of an edge dislocation and ignoring the point defects that are inside. The atoms on the surface are known to have higher-strain than the atoms inside the loop [11]. Many of the experiments, and material properties are known to correlate well with the surface atoms of the defect rather than the total number of point defects. We can see that when only the surface defects are counted different potentials and energies show similar values and trends. The simulations that produce bigger defect clusters observe a decrease in the defects when only the surface defects are counted. For this reason, the values for DND-BN potential see more reduction than the SNAP potential. The SNAP potential at 20 keV gets least affected as it has small defects and very few edge dislocation loops. We will see this in detail in later sections on SIA defect size distribution and morphology details.

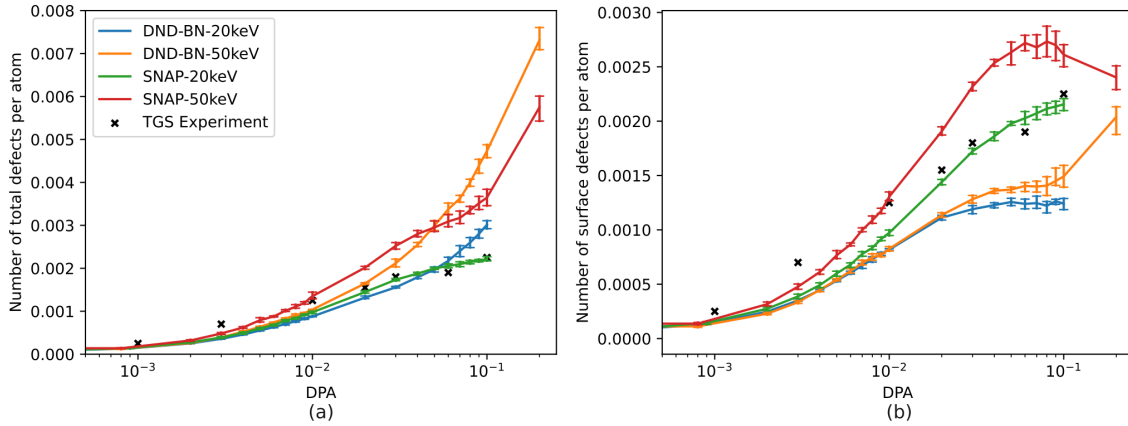


Figure 1: At various dpa, the (a) number of total point defects per atom (b) number of single point defects and defects on the surface of a cluster for the four cases specified in Table.1.

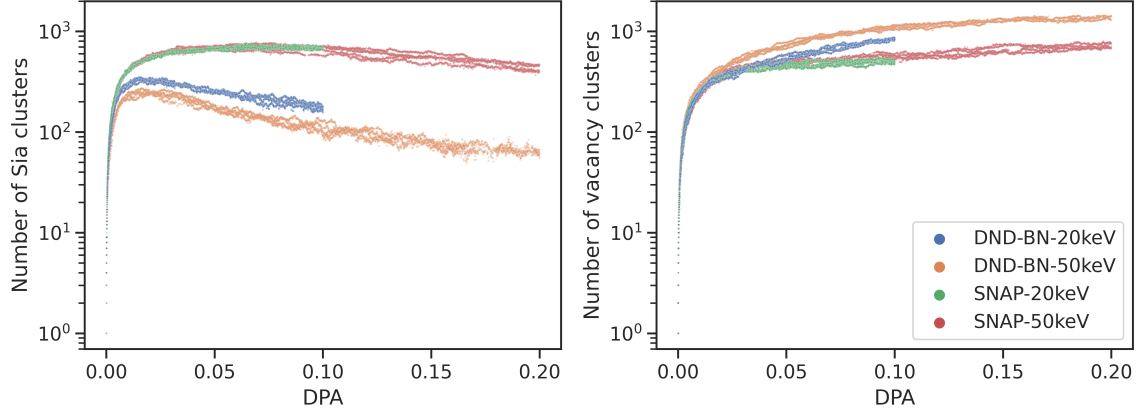


Figure 2: Variation of the number of defect clusters of (a) SIA and (b) Vacancy, with dpa for the four cases specified in Table.1

Fig.1 also shows the number of defects estimated by the transient grating spectroscopy [33] experiment for the 20 MeV self-ion irradiation of tungsten. The Transient Grating Spectroscopy experiment is indicative of the number of surface defects rather than the total defects [33]. All the simulations show a decent match with the experimental results. The SNAP potential at 20 keV shows the best match with the experiment. The DND-BN potential shows slightly lower number of surface defects. However, both the potentials seems to be approaching the experimental values at 0.2 dpa.

We find that the number of total defects at different dpa differ based on energy of the PKA but the total number of surface defects show similar trends. Even if the surface defects rise at certain point they start to decrease as the defect clusters grow in size and start to merge together. The saturation point of 0.002 defects per atom matches that of the experiments [33]. The total defects deviate largely based on the IAP used, however the surface defects again seems to be converging as the dpa increases. The experiment is conducted at 20 MeV. A very high energy PKA results in a combination of subcascades of lower energy.

Fig.2 shows the variation in the number of SIA and vacancy clusters as a function of dpa. The number of SIA clusters for DND-BN start to decrease while for SNAP the values only saturate. The decrease in clusters in DND-BN is due to the big SIA clusters in DND-BN which start to merge together with the increase in defect density. There is a quantitative separation based on the IAP rather than the PKA energy as was seen in the case of number of defects.

Fig.3 shows the number density of dislocations greater than 1.5 nm (or having defect count greater than 30) which are big enough to be observed in a TEM [31]. The defect density of such defects in SNAP at 20 keV remains lower compared to others. In other cases the defects increase with dose and then start to decrease as the defect clusters grow in size and start to merge together. Since, biggest defects are formed in DND-BN simulation at 50 keV, the saturation appears earliest (at around 0.4 dpa) in it. The experimental values from a TEM experiment performed by 150keV self ion irradiation [31] are also shown. The values for SNAP potential at 50 keV perfectly matches initially and again appear to be approaching the experimental value at 0.2 dpa with an over-estimation in the mid dpa range. The values rise till around 0.1 dpa and then start to decrease. The decrease in loop density is due to merging of defects to form dislocation strings and networks. The decrease of loop density starting at around 0.1 dpa and then saturating by 0.2 dpa at a much lower value agrees well with the recent TEM experiment [32]. The value for loop density significantly differs for 20 keV and 50 keV. The experiment values in the plot are for 150keV self ion-irradiation which is close

to the subcascade threshold of W [13]. A 150 keV cascade would break into combination of lower energy sub-cascades in different proportions [13]. In such a case, the SNAP potential's slightly lesser values of loop density at 20 keV and slightly higher values at 50 keV compared to the experiment seems to be balancing out for a better agreement than the consistently higher estimations of DND-BN at both the energies.

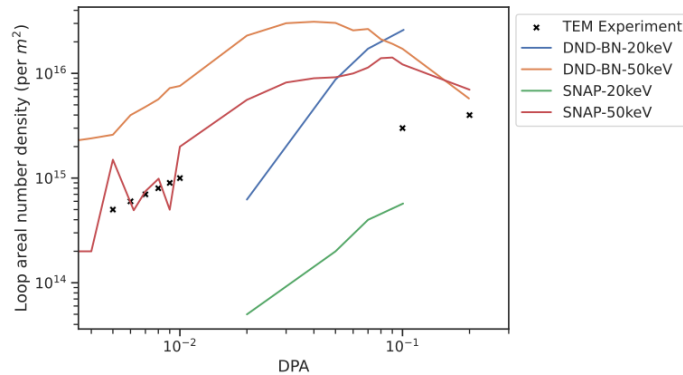


Figure 3: Loop density of TEM-visible defects as a function of dpa for the four cases specified in Table.1

### 3.2. In-cluster defects

Fig.4 shows in-cluster SIAs and vacancies as a function of dpa. From Fig.4 (a) it can be seen that the percentage of interstitials in clusters quickly rises and reaches a value greater than 95 % before 0.01 dpa for SNAP and by 0.04 dpa for DND-BN. The rising curves are separated by IAP type rather than the PKA energy. For the in-cluster vacancies case shown in Fig.4 (b), there is a gradual rise with dpa. Unlike the in-cluster interstitials case, there is a well defined separation in the variation of the percentage of vacancies in clusters for both the PKA energies and for the IAP. The vacancies also show greater variability for different simulation trials. In general the SNAP potential shows a larger number of in-cluster vacancies.

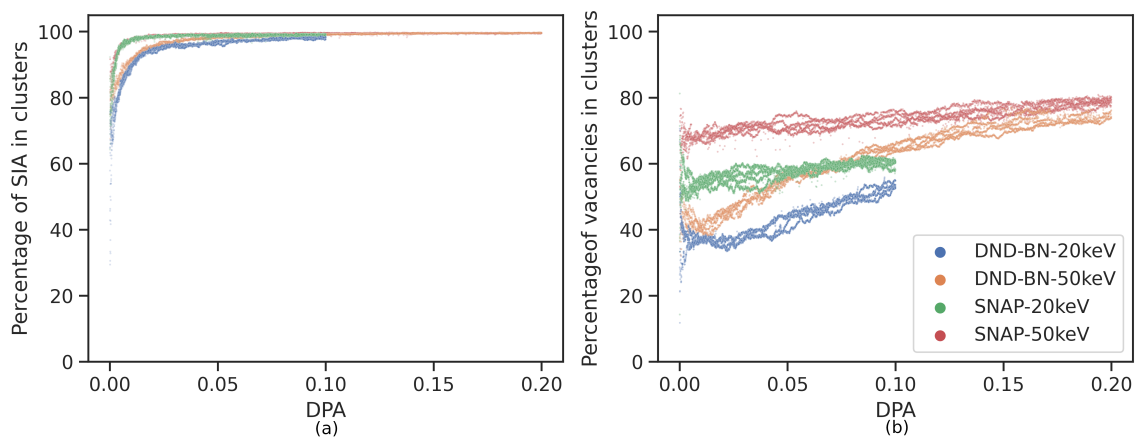


Figure 4: Variation of the number of in-cluster (a) SIAs and (b) Vacancies with dpa for the four cases specified in Table.1

### 3.3. Vacancy Size Distribution

Fig.5 shows the vacancy cluster size distribution for all the vacancy clusters with size more than 5 number of vacancies. As the dpa increases the maximum vacancy size and the counts for all the sizes both grow in all the cases. The vacancy sizes for the same dpa at different energies are vastly different. The 50keV energy cases for both the IAPs have bigger vacancy clusters compared to 20keV. This is expected because at both these energies, W still prefers single sub-cascade [13] and the 50keV single sub-cascade will have a bigger central core of vacant sites. It can be seen that the distributions of SNAP IAP have slightly fatter tails signifying tendency to have more of bigger vacancy clusters. This is contrary to the SIA cluster size distribution as we will show in the following results.

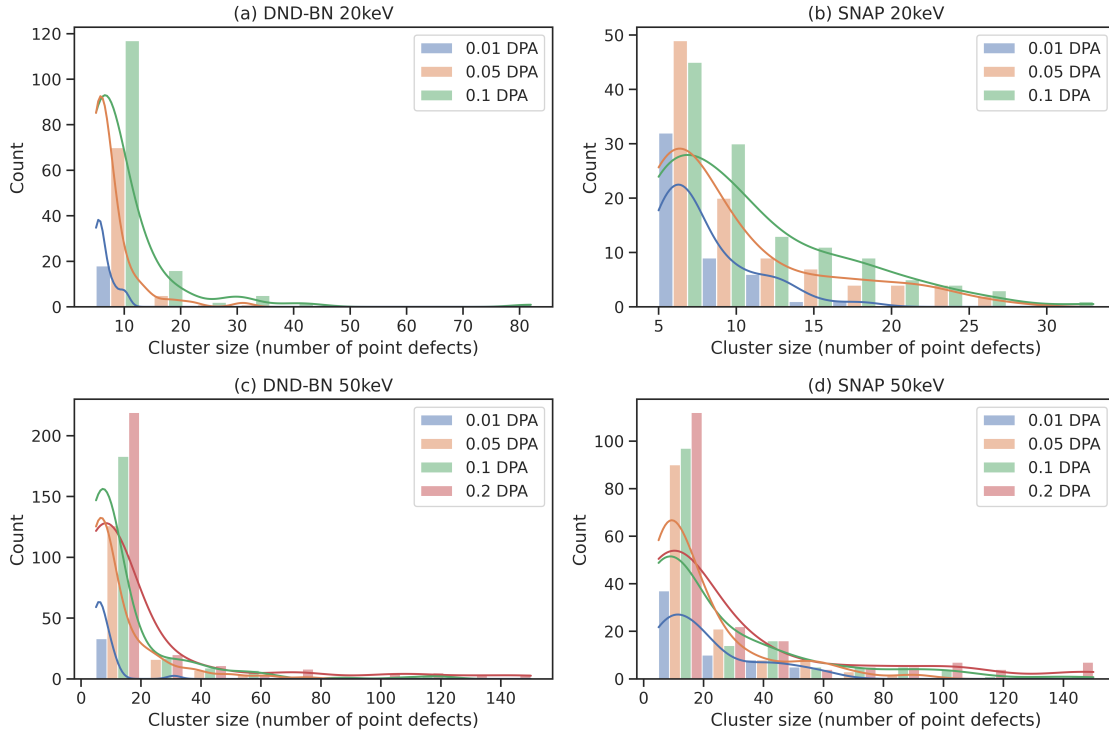


Figure 5: Vacancy cluster size distribution at 0.01, 0.05 and 0.1 dpa for the four cases specified in Table.1

### 3.4. Defect Morphologies

Fig.6 shows the SIA defects in the simulation box at different dpa. The SIA are coloured based on the orientation of dumbbells/crowdions as found using SaVi algorithm [11]. The bigger clusters of parallel  $\langle 111 \rangle$  and  $\langle 100 \rangle$  dumbbells/crowdions form the edge dislocations with burgers vector of  $1/2\langle 111 \rangle$  and  $\langle 100 \rangle$ , respectively. The  $\langle 110 \rangle$  dumbbells sometimes appear at the interface between a multi-component dislocation (a cluster of two or more dislocations) but mostly they form the C15 like rings or their basis [11]. Fig.7 shows a typical C15 3d ring defect. A defect can be composed of multiple such ring units. The frames in the Fig.6, qualitatively show the differences in morphology of SIAs in the four cases. The SNAP IAP

forms lots of small C15 like rings while in case of DND-BN we observe bigger  $\langle 111 \rangle$  and  $\langle 100 \rangle$  defects being formed as the dpa increases. The presence of rings in SNAP can be noted at high dpa as well.

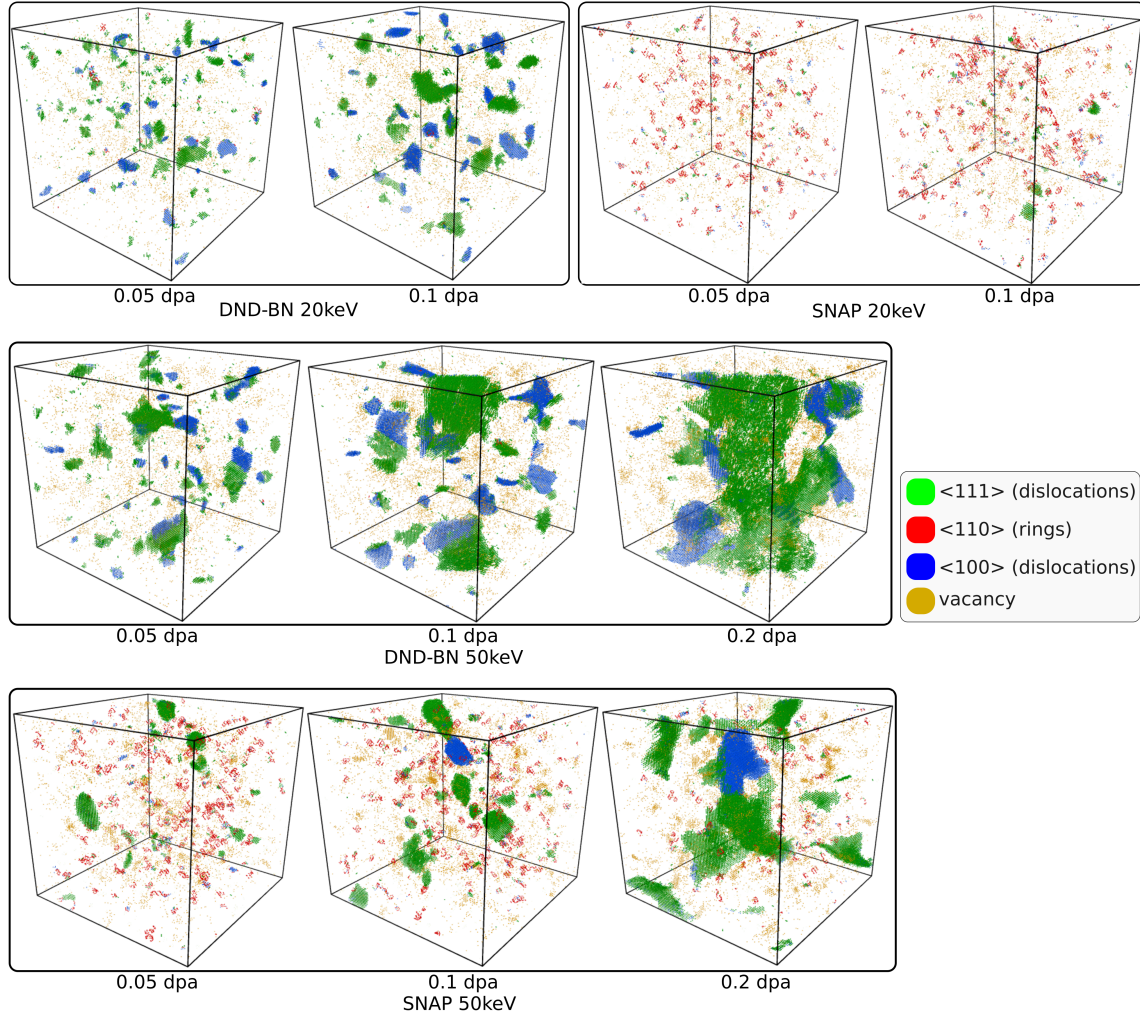


Figure 6: SIA defects at different dpa in the simulation box. The colours show the SIA dumbbell/crowdion orientation. The bigger clusters of  $\langle 111 \rangle$  and  $\langle 100 \rangle$  dumbbells/crowdions form the edge dislocations with the respective burgers vector. Almost all the  $\langle 110 \rangle$  dumbbells/crowdions form C15 like rings. For the same dpa, the density and sizes of defects at higher energy are more. SNAP shows high number of rings while bigger dislocations dominate in DND-BN.

The number of  $\langle 100 \rangle$  dislocations increase in DND-BN. The  $\langle 100 \rangle$  dislocations can get formed by the interaction of two non-collinear dislocations [31]. The diffusion and creation of more dislocations results in dislocations being combined to form bigger multi-dislocations and dislocation network [32]. This results in reduction of the number of surface defects and the number of clusters as shown earlier in Fig.1 and Fig.3. The sizes of the defects for 20 keV at 0.1 dpa match well with that of 50 keV at 0.05 dpa for the same potential. This is due to the bigger clusters being formed right after a 50 keV collision cascade as compared

to a 20 keV collision cascade. This supports the variation of loop density of TEM-visible loops for the two energies in Fig.3.

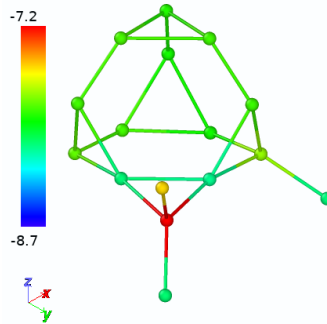


Figure 7: A typical C15 ring (denoted by @) like structure observed in tungsten. The color-map represents the potential energy of the atoms (in eV) - visible in color in the digital version of this article.

Fig.8 and Fig.9 quantify the above observations, showing the distribution of different morphologies and their mean sizes, respectively. We have resolved the different morphological components in a defect composed of multiple dislocations or dislocation and ring component. Different morphologies are represented by different ASCII letters for the figure labels. || signifies clusters with dumbbells/crowdions arranged in parallel configuration which form  $1/2 \langle 111 \rangle$  and  $\langle 100 \rangle$  edge dislocations in W. The symbol @ signifies C-15 like rings and its basis configurations. There are also mixed morphologies defects with multiple components. We distinguish between dislocations that are part of a mixed dislocation defect (cluster having multiple loops) and defects that are composed of homogeneously one dislocation loop. The symbol /// is for defects composed of two or more dislocations in different orientations. In the Figure legend, the symbol || - 111 : /// represents the number of defects that form  $\langle 111 \rangle$  edge dislocation and are part of a multi-component dislocation while || - 111 : || is the number of defects that form pure  $\langle 111 \rangle$  dislocation. The symbol || - 111 : @@ is for the configuration that form  $\langle 111 \rangle$  dislocation while also being attached to a ring @. The properties such as diffusion, stability and interaction of the same component || - 111 can vary in the above three cases.

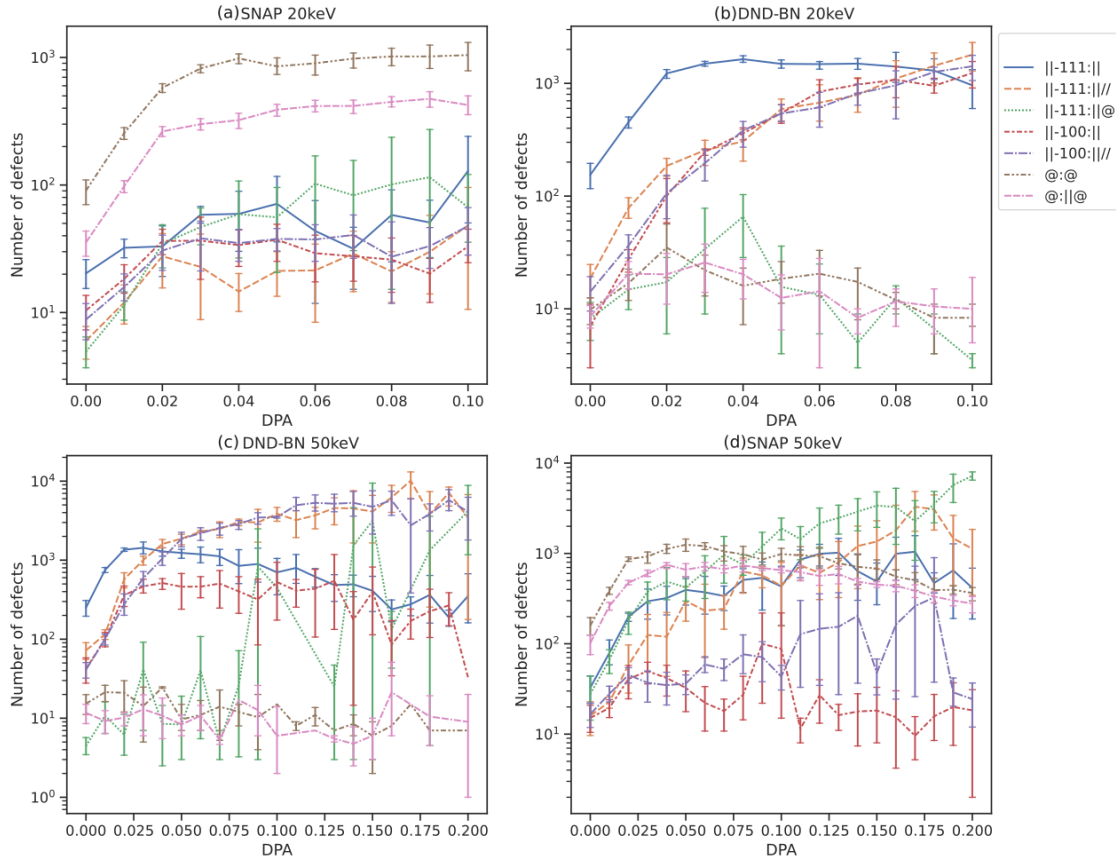


Figure 8: Variation in the number of defect clusters of various types with dpa for the four cases specified in Table.1. The symbols in the legend represent morphology of single dislocation  $\parallel$  with  $\langle 100 \rangle$  or  $\langle 111 \rangle$  Burgers vector or a ring  $@$ . These may also appear in mixed defect configurations such as dislocation-ring ( $\parallel@$ ) or multi-dislocation ( $\parallel//$ ).

The number of defects in different morphologies remain similar for the two energies of same IAP, whereas notable difference exists across the two IAPs. Fig.8 shows that the SNAP IAP results in significantly higher number of ring like structures. The rings remain high through out the DPA range. The DND-BN potential in contrast shows very few ring like structures and the micro-structure is dominated by the edge dislocations  $\parallel$ . Initially, the  $1/2\langle 111 \rangle$  edge-dislocations in pure ( $\parallel$ ) as well as mixed  $\parallel//$  defects are highest however at higher dpa the  $\langle 100 \rangle$  dislocations become dominant and pure  $\langle 111 \rangle$  dislocations start to drop. In contrast, SNAP IAP shows very less  $\langle 100 \rangle$  edge-dislocations.

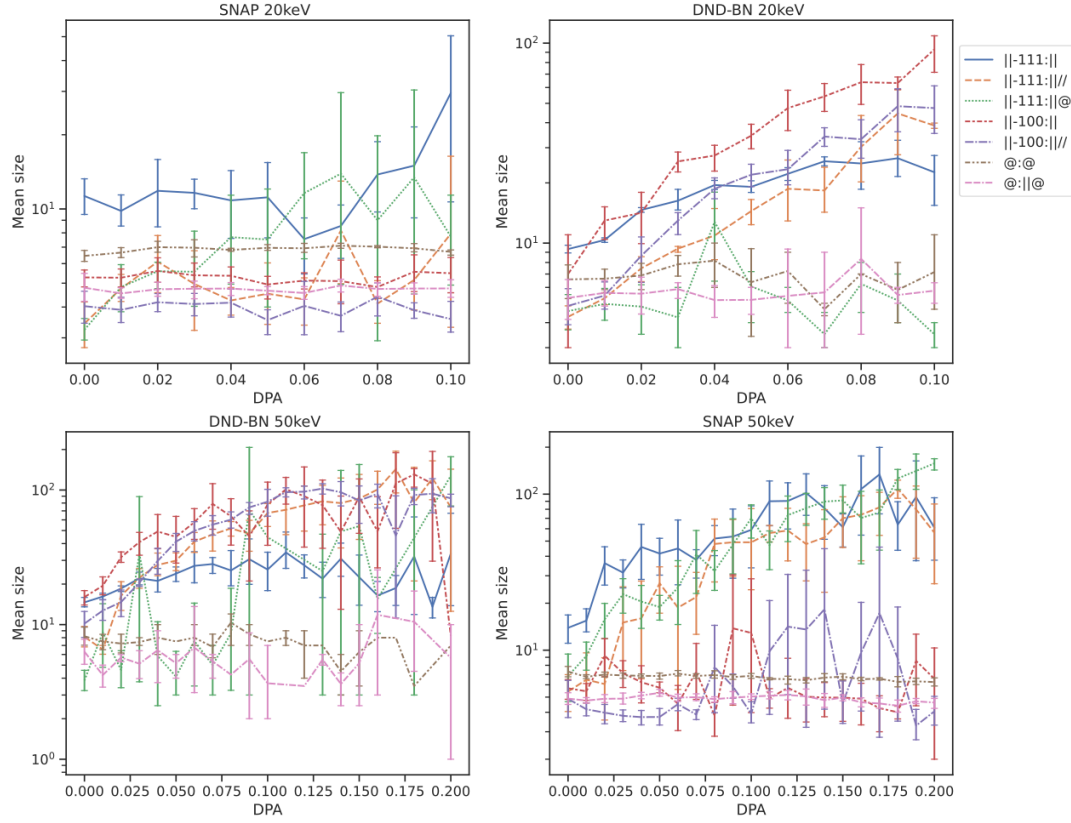


Figure 9: Variation in the mean size of SIA defect clusters of various types with dpa for the four cases specified in Table.1. Here the size refers to the number of SIA constituting a defect cluster. The symbols in the legend represent morphology of single dislocation  $\parallel$  with  $\langle 100 \rangle$  or  $\langle 111 \rangle$  Burgers vector or a ring  $@$ . These may also appear in mixed defect configurations such as dislocation-ring ( $\parallel@$ ) or multi-dislocation ( $\parallel//$ ).

The mean sizes of the SIA defect clusters in various morphologies as a function of dpa in fig.9 shows that the pure  $\langle 111 \rangle$  parallel defects ( $\parallel - 111 : \parallel$ ) that form glissile  $1/2 \langle 111 \rangle$  edge dislocations have a mean size of few tens of defects in all the four cases. The mean size of pure as well as mixed  $\langle 100 \rangle$  dislocation component is slightly higher than  $\langle 111 \rangle$  in DND-BN. In SNAP  $\parallel - 100 : \parallel$  rarely gets formed. The small  $\langle 100 \rangle$  edge dislocations defects are not stable in W [21] as a result the mean size of  $\langle 100 \rangle$  dislocations ( $\parallel - 100$ ) is higher in DND-BN than the  $\langle 111 \rangle$  parallel defects which includes bigger  $\langle 111 \rangle$  edge dislocations as well as many small parallel pairs, triplets etc. of dumbbells which form very often with every collision cascade.

For SNAP, the mean size of rings remain less than 10 although the maximum is a few tens of point defects. A good number of bigger  $\langle 111 \rangle$  edge dislocations appear in conjunction with a ring component

( $\parallel - 111 : \parallel @$ ). It is seen that for both the IAPs the C15 ring like structures ( $@$  and  $@\parallel$ ) are small while the  $\langle 111 \rangle$  and  $\langle 100 \rangle$  defects are relatively much bigger, especially for the DND-BN potential. This matches the trend of larger sized loop formation at higher dpa as seen in experiments [32, 38].

The trend of mean sizes for dislocations ( $\parallel$ ) are slightly different for the two energies. For DND-BN at 20keV, the sizes of  $\langle 100 \rangle$  and  $\langle 111 \rangle$  in multi-component dislocation defect ( $\parallel//$ ) start at lower value and increase gradually in size with DPA while at 50 keV the sizes of these morphologies get comparatively higher from the beginning. For SNAP, at 20keV the mean sizes remain slightly lower when compared with 50keV.

### 3.5. Swelling

Fig.10 shows the expansion or swelling of the simulation box as a function of dpa. The increase in simulation box size is more significant in SNAP IAP than DND-BN. The swelling in 50 keV is more for both the potentials. The experimental values for swelling at different doses and temperatures is reported to be in the range of 0.2 to 0.4% [39, 40]. The swelling suggested by DND-BN is quite low while SNAP potential especially at 50keV is closer to the experimental results.

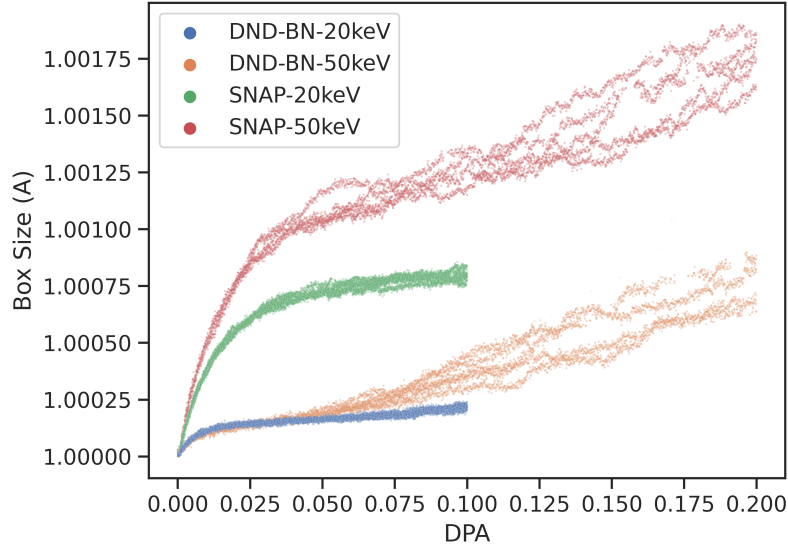


Figure 10: Fractional increase in the simulation box size as a function of dpa for both the potentials and both the energies.

## 4. Discussion

The SNAP and DND-BN potentials that we have used in our study show significant differences in defect morphologies and sizes. The SNAP machine learning potential which can be considered quantum accurate, produces high number of smaller, stable and sessile ring defect clusters in addition to  $\langle 111 \rangle$  dislocation loops while DND-BN potential mainly produces big  $\langle 111 \rangle$  as well as  $\langle 100 \rangle$  dislocations. Despite these differences when we look at the damage properties that can be measured and are known to correlate well with the material properties, such as the number density of surface point defects and the number of TEM-visible

defect loops, the two potentials show similar trends (as shown in Fig.1 and Fig.3). The SNAP potential does show a slightly better match with the experimental values of surface defect density and swelling which suggests that its prediction of high number of stable rings is likely to be accurate. Since, these rings are relatively small, their signatures need to be exclusively looked for in experiments. A high number of sessile rings can restrict the diffusion of mobile defects. An interesting investigation would be to observe how the defects with different mobility will interact with each other and affect the microstructural properties with time evolution.

The irradiation induced damage in materials is quantified by the number of displacements per atom (dpa) since many of the material properties are known to correlate well with the dpa irrespective of the energy of the incident particle [24]. The total number of surface defects show similar trends with dpa for both the PKA energies and does not show significant deviation based on the IAP. The number of surface defects are rarely noted in the literature when comparing collision cascades carried out with different potentials or materials. The current study suggests that the number of surface defects is an important parameter for such studies.

## 5. Conclusions

MD simulations of successive collision cascades have been carried out in tungsten at PKA energies of 20 keV and 50 keV using an EAM and a ML based inter-atomic potential. For both the potentials, five sample simulations were carried out with successive PKAs reaching a dose of 0.1 and 0.2 dpa for 20keV and 50keV, respectively. Various properties such as the the number density of defect clusters and in-cluster SIAs is same for both the PKA energies while the SIA and vacancy cluster sizes are notably high at higher energy (Fig.5 and Fig.9). The number of surface defects are observed to saturate at the same level as experiments irrespective of energy of the PKA or the potential used.

The defect morphology of the two potentials are significantly different. The SNAP potential produces smaller, stable and sessile C15-like ring defect clusters in addition to  $\langle 111 \rangle$  dislocation loops while the EAM potential produces bigger  $\langle 100 \rangle$  and  $\langle 111 \rangle$  dislocations. The SNAP potential which is considered more closer to ab-initio calculations also shows a better overall match with the experimental values of the swelling, number of surface defects and number density of TEM visible defects. Very high number of  $\langle 100 \rangle$  dislocation loops suggested in DND-BN potential at high dpa also appears to be an over-estimation compared to the current experiments [31]. The predictions of the SNAP potential for a high number of stable rings is very likely to have practical considerations and the existence of such rings must be investigated further. The presence of small sessile defects can have significant impact on defect evolution and material properties.

## Acknowledgements

We acknowledge the HPC team at CAD for the HPC maintenance and for support in installing LAMMPS.

## References

- [1] J. B. Gibson, A. N. Goland, M. Milgram, G. H. Vineyard, Dynamics of radiation damage, *Phys. Rev.* 120 (1960) 1229–1253. doi : 10.1103/PhysRev.120.1229.
- [2] S. Zinkle, 1.03 - radiation-induced effects on microstructure\*, in: R. J. Konings (Ed.), *Comprehensive Nuclear Materials*, Elsevier, Oxford, 2012, pp. 65 – 98. doi : <https://doi.org/10.1016/B978-0-08-056033-5.00003-3>.

- [3] K. Nordlund, Historical review of computer simulation of radiation effects in materials, *Journal of Nuclear Materials* 520 (2019) 273–295. doi:<https://doi.org/10.1016/j.jnucmat.2019.04.028>.  
URL <https://www.sciencedirect.com/science/article/pii/S0022311518314703>
- [4] R. Stoller, S. Golubov, C. Domain, C. Becquart, Mean field rate theory and object kinetic monte carlo: A comparison of kinetic models, *Journal of Nuclear Materials* 382 (2) (2008) 77 – 90, *microstructural Processes in Irradiated Materials*. doi:<http://dx.doi.org/10.1016/j.jnucmat.2008.08.047>.
- [5] R. Stoller, 1.11 - primary radiation damage formation, in: R. J. Konings (Ed.), *Comprehensive Nuclear Materials*, Elsevier, Oxford, 2012, pp. 293 – 332. doi:<https://doi.org/10.1016/B978-0-08-056033-5.00027-6>.
- [6] D. Bacon, F. Gao, Y. Osetsky, The primary damage state in fcc, bcc and hcp metals as seen in molecular dynamics simulations, *Journal of Nuclear Materials* 276 (1) (2000) 1–12. doi:[https://doi.org/10.1016/S0022-3115\(99\)00165-8](https://doi.org/10.1016/S0022-3115(99)00165-8).  
URL <https://www.sciencedirect.com/science/article/pii/S0022311599001658>
- [7] L. Malerba, Molecular dynamics simulation of displacement cascades in  $\alpha$ -fe: A critical review, *Journal of Nuclear Materials* 351 (1) (2006) 28–38, *proceedings of the Symposium on Microstructural Processes in Irradiated Materials*. doi:<https://doi.org/10.1016/j.jnucmat.2006.02.023>.  
URL <https://www.sciencedirect.com/science/article/pii/S0022311506000638>
- [8] Cascadesdb is a database of molecular dynamics simulations of collision cascades, developed by the international atomic energy agency.  
URL <https://cascadesdb.org/>
- [9] A. De Backer, C. S. Becquart, P. Olsson, C. Domain, Modelling the primary damage in fe and w: influence of the short-range interactions on the cascade properties: Part 2 – multivariate multiple linear regression analysis of displacement cascades, *Journal of Nuclear Materials* 549 (2021) 152887. doi:<https://doi.org/10.1016/j.jnucmat.2021.152887>.  
URL <https://www.sciencedirect.com/science/article/pii/S0022311521001100>
- [10] U. Bhardwaj, A. E. Sand, M. Warriar, Classification of clusters in collision cascades, *Computational Materials Science* 172 (2020) 109364. doi:<https://doi.org/10.1016/j.commatsci.2019.109364>.  
URL <https://www.sciencedirect.com/science/article/pii/S0927025619306639>
- [11] U. Bhardwaj, A. E. Sand, M. Warriar, Graph theory based approach to characterize self interstitial defect morphology, *Computational Materials Science* 195 (2021) 110474. doi:<https://doi.org/10.1016/j.commatsci.2021.110474>.  
URL <https://www.sciencedirect.com/science/article/pii/S0927025621001993>
- [12] U. Bhardwaj, H. Hemanu, M. Warriar, N. Semwal, K. Ali, A. Arya, Saransh : Software suite to study molecular dynamics simulations of collision cascades, *Journal of Open Source Software* 4(41) (2019) 1461. doi:<https://doi.org/10.21105/joss.01461>.
- [13] U. Bhardwaj, M. Warriar, Identifying subcascades from the primary damage state of collision cascades (2023). arXiv:2306.04975.

- [14] J. Byggmästar, F. Granberg, K. Nordlund, Effects of the short-range repulsive potential on cascade damage in iron, *Journal of Nuclear Materials* 508 (2018) 530–539. doi:<https://doi.org/10.1016/j.jnucmat.2018.06.005>.  
URL <https://www.sciencedirect.com/science/article/pii/S0022311518305166>
- [15] C. S. Becquart, A. Souidi, M. Hou, Relation between the interaction potential, replacement collision sequences, and collision cascade expansion in iron, *Phys. Rev. B* 66 (2002) 134104. doi:[10.1103/PhysRevB.66.134104](https://doi.org/10.1103/PhysRevB.66.134104).  
URL <https://link.aps.org/doi/10.1103/PhysRevB.66.134104>
- [16] D. Terentyev, C. Lagerstedt, P. Olsson, K. Nordlund, J. Wallenius, C. Becquart, L. Malerba, Effect of the interatomic potential on the features of displacement cascades in  $\alpha$ -Fe: A molecular dynamics study, *Journal of Nuclear Materials* 351 (1) (2006) 65–77, proceedings of the Symposium on Microstructural Processes in Irradiated Materials. doi:<https://doi.org/10.1016/j.jnucmat.2006.02.020>.  
URL <https://www.sciencedirect.com/science/article/pii/S0022311506000675>
- [17] A. Sand, J. Dequeker, C. Becquart, C. Domain, K. Nordlund, Non-equilibrium properties of interatomic potentials in cascade simulations in tungsten, *Journal of Nuclear Materials* 470 (2016) 119–127. doi:<https://doi.org/10.1016/j.jnucmat.2015.12.012>.  
URL <https://www.sciencedirect.com/science/article/pii/S0022311515303810>
- [18] U. Bhardwaj, A. E. Sand, M. Warriar, Comparison of sia defect morphologies from different interatomic potentials for collision cascades in w, *Modelling and Simulation in Materials Science and Engineering* 29 (6) (2021) 065015. doi:[10.1088/1361-651X/ac095d](https://doi.org/10.1088/1361-651X/ac095d).  
URL <https://dx.doi.org/10.1088/1361-651X/ac095d>
- [19] C. Domain, C. Becquart, L. Malerba, Simulation of radiation damage in Fe alloys: an object kinetic monte carlo approach, *Journal of Nuclear Materials* 335 (1) (2004) 121 – 145. doi:[http://dx.doi.org/10.1016/j.jnucmat.2004.07.037](https://doi.org/10.1016/j.jnucmat.2004.07.037).
- [20] C. Becquart, A. Barbu, J. Bocquet, M. Caturla, C. Domain, C.-C. Fu, S. Golubov, M. Hou, L. Malerba, C. Ortiz, A. Souidi, R. Stoller, Modeling the long-term evolution of the primary damage in ferritic alloys using coarse-grained methods, *Journal of Nuclear Materials* 406 (1) (2010) 39–54, FP6 IP PERFECT Project: Prediction of Irradiation Damage Effects in Reactor Components. doi:<https://doi.org/10.1016/j.jnucmat.2010.05.019>.  
URL <https://www.sciencedirect.com/science/article/pii/S002231151000231X>
- [21] U. Bhardwaj, A. E. Sand, M. Warriar, Stability of  $\{100\}$  dislocations formed in w collision cascades, *Journal of Nucl. Mater.* 569 (2022) 153938.
- [22] L. Liu, N. Gao, Y. Chen, R. Qiu, W. Hu, F. Gao, H. Deng, Formation mechanism of  $\langle 111 \rangle$  interstitial dislocation loops from irradiation-induced c15 clusters in tungsten, *Phys. Rev. Mater.* 5 (2021) 093605. doi:[10.1103/PhysRevMaterials.5.093605](https://doi.org/10.1103/PhysRevMaterials.5.093605).  
URL <https://link.aps.org/doi/10.1103/PhysRevMaterials.5.093605>
- [23] A. Standard, E693-94, Standard practice for characterising neutron exposure in iron and low alloy steels in terms of displacements per atom (dpa).

- [24] G. Was, R. Averback, 1.07 - Radiation Damage Using Ion Beams, Vol. 1-5, Elsevier, 2012, pp. 195–221, publisher Copyright: © 2012 Elsevier Ltd. All rights reserved. doi:10.1016/B978-0-08-056033-5.00007-0.
- [25] M. Norgett, M. Robinson, I. Torrens, A proposed method of calculating displacement dose rates, Nuclear Engineering and Design 33 (1) (1975) 50 – 54. doi:http://dx.doi.org/10.1016/0029-5493(75)90035-7.
- [26] K. Nordlund, S. J. Zinkle, A. E. Sand, F. Granberg, et al., Improving atomic displacement and replacement calculations with physically realistic damage models, Nature Communications 9 (2018) 1084.
- [27] R. Stoller, K. Nordlund, S. Simakov, Summary report of the technical meeting on primary radiation damage: from nuclear reaction to point defects, INDC International Nuclear Data Committee Report INDC-NDS-0624.
- [28] R. Stoller, L. R. Greenwood, S. Simakov, Summary report of the first research coordination meeting on primary radiation damage cross sections, INDC International Nuclear Data Committee Report INDC-NDS-0648.
- [29] A. R. Warwick, M. Boleininger, S. L. Dudarev, Microstructural complexity and dimensional changes in heavily irradiated zirconium, Phys. Rev. Mater. 5 (2021) 113604. doi:10.1103/PhysRevMaterials.5.113604.  
URL <https://link.aps.org/doi/10.1103/PhysRevMaterials.5.113604>
- [30] D. R. Mason, F. Granberg, M. Boleininger, T. Schwarz-Selinger, K. Nordlund, S. L. Dudarev, Parameter-free quantitative simulation of high-dose microstructure and hydrogen retention in ion-irradiated tungsten, Phys. Rev. Mater. 5 (2021) 095403. doi:10.1103/PhysRevMaterials.5.095403.  
URL <https://link.aps.org/doi/10.1103/PhysRevMaterials.5.095403>
- [31] X. Yi, M. L. Jenkins, M. A. Kirk, Z. Zhou, S. G. Roberts, In-situ tem studies of 150 keV w+ ion irradiated w and w-alloys: Damage production and microstructural evolution, Acta Materialia 112 (2016) 105–120. doi:https://doi.org/10.1016/j.actamat.2016.03.051.  
URL <https://www.sciencedirect.com/science/article/pii/S135964541630204X>
- [32] S. Wang, W. Guo, T. Schwarz-Selinger, Y. Yuan, L. Ge, L. Cheng, X. Zhang, X. Cao, E. Fu, G.-H. Lu, Dynamic equilibrium of displacement damage defects in heavy-ion irradiated tungsten, Acta Materialia 244 (2023) 118578.
- [33] A. Reza, H. Yu, K. Mizohata, F. Hofmann, Thermal diffusivity degradation and point defect density in self-ion implanted tungsten, Acta Materialia 193 (2020) 270–279. doi:https://doi.org/10.1016/j.actamat.2020.03.034.  
URL <https://www.sciencedirect.com/science/article/pii/S1359645420302214>
- [34] C. Björkas, K. Nordlund, S. Dudarev, Modelling radiation effects using the ab-initio based tungsten and vanadium potentials, Nuclear Instruments and Methods in Physics Research Section B: Beam Interactions with Materials and Atoms 267 (18) (2009) 3204 – 3208, proceedings of the Ninth International Conference on Computer Simulation of Radiation Effects in Solids. doi:http://dx.doi.org/10.1016/j.nimb.2009.06.123.

- [35] M. A. Wood, A. P. Thompson, Quantum-accurate molecular dynamics potential for tungsten (2017). arXiv:1702.07042.
- [36] J. F. Ziegler, J. P. Biersack, The stopping and range of ions in matter, in: *Treatise on Heavy-Ion Science*, Springer, 1985, pp. 93–129.
- [37] H. Hemani, A. Majalee, U. Bhardwaj, A. Arya, K. Nordlund, M. Warriar, Inclusion and validation of electronic stopping in the open source lammmps code (2020). arXiv:2005.11940.
- [38] R. Rayaprolu, S. Möller, R. Abernethy, M. Rasinski, J. Haley, C. Linsmeier, Indentation testing on 3 mev proton irradiated tungsten, *Nuclear Materials and Energy* 25 (2020) 100776. doi:<https://doi.org/10.1016/j.nme.2020.100776>. URL <https://www.sciencedirect.com/science/article/pii/S2352179120300521>
- [39] O. El-Atwani, E. Esquivel, M. Efe, E. Aydogan, Y. Wang, E. Martinez, S. A. Maloy, Loop and void damage during heavy ion irradiation on nanocrystalline and coarse grained tungsten: Microstructure, effect of dpa rate, temperature, and grain size, *Acta Materialia* 149 (2018) 206–219.
- [40] D. Nguyen-Manh, J. S. Wróbel, M. Klimenkov, M. J. Lloyd, L. Messina, S. L. Dudarev, First-principles model for voids decorated by transmutation solutes: Short-range order effects and application to neutron irradiated tungsten, *Physical Review Materials* 5 (6) (2021) 065401.